ChemPubSoc Europe

DOI: 10.1002/cphc.201601279

CHEMPHYSCHEM Articles

Special Issue

Optical and Magnetic Properties of Fe Nanoparticles Fabricated by Femtosecond Laser Ablation in Organic and Inorganic Solvents

Jesica M. J. Santillán,[a] David Muñetón Arboleda,[a] Diego F. Coral,[b, c] Marcela B. Fernández van Raap,[b, c] Diego Muraca,[d] Daniel C. Schinca,*[a, e] and Lucía B. Scaffardi[a, e]

Magnetic nanoparticles have attracted much interest due to their broad applications in biomedicine and pollutant remediation. In this work, the optical, magnetic, and structural characteristics of colloids produced by ultrashort pulsed laser ablation of a solid Fe target were studied in four different media: HPLC water, an aqueous solution of trisodium citrate, acetone, and ethanol. Optical extinction spectroscopy revealed an absorption band in the UV region for all, in contrast to the results obtained with nanosecond lasers. Micro-Raman spectroscopy showed that the samples are heterogeneous in their composition, with hematite, maghemite, and magnetite nanoparticles in all four solvents. Similar results were obtained by electron diffraction, which also found α-Fe. Magnetic properties were studied by vibrating-sample magnetometry, and showed nanoparticles in the superparamagnetic state. Under certain experimental conditions, submicrometer-sized iron oxide nanoparticles agglomerate into fractal patterns that show self-similar properties. Self-assembled annular structures on the nanometer scale were also observed and are reported for the first time.

1. Introduction

One of the most active topics in nanotechnology is the synthesis, characterization, and functionalization of magnetic nanoparticles (NPs). The interest in magnetic NPs is due to their broad applications in areas such as diagnosis and therapeutics in biomedicine (e.g., magnetic targeting of genes and cells, magnetic hyperthermia),[1–3] contrast agents for magnetic resonance imaging,[4] drug delivery,[5] and remediation of metal pollutants.[6,7] The variety of magnetic NP fabrication techniques is quite large, and includes chemical precipitation,[8,9] sol–gel processes,[10,11] and hydrothermal,[12] microemulsion,[13] electrochemical,[14] and sonochemical techniques.[15]

Laser ablation is the removal of material from a target of interest by direct absorption of laser energy. Pulsed laser ablation of solids in liquids has emerged in recent years as a reliable, rapid, and green method for preparing NPs in suspensions, which are generally spherical in shape. When pulsed laser ablation is performed on a metal target, different types of NPs may be formed, such as bare metal core, metal core/oxide shell, and hollow metal.[16,17] Many authors[18–23] have used this approach, as well as with coprecipitation, to study magnetic, optical, and structural properties of colloidal suspensions obtained after nanosecond pulsed laser ablation of Fe targets in a variety of solvents.

Liu et al.[18] reported the fabrication of FeO NPs by pulsed laser ablation of a pure iron plate in an aqueous solution of polyvinylpyrrolidone (PVP). Particle size could be controlled by means of the PVP concentration due to the capping effect and repulsive interaction of the solvent. Vitta et al.[19] obtained α-Fe NPs using nanosecond laser ablation of an Fe target in an aqueous solution of sodium dodecyl sulfate. Characterization of these NPs proved that their morphology consists of a core of zero-valent iron surrounded by oxidized species, which prevent further oxidation. Besides, optical extinction spectra showed an absorption peak that depends on the pH value of the solvent. Amendola et al.[20,21] showed that laser ablation of an iron target in different organic liquids is a suitable method for obtaining a variety of magnetic nanostructures, including

[a] J. M. J. Santillán, D. Muñetón Arboleda, D. C. Schinca, L. B. Scaffardi
Centro de Investigaciones Ópticas (CIOp)
(CONICET La Plata-CIC-UNLP), CC3 (1897)
Gonnet, La Plata, Buenos Aires (Argentina)
E-mail: daniels@ciop.unlp.edu.ar
lucias@ciop.unlp.edu.ar

[b] D. F. Coral, M. B. Fernández van Raap
Instituto de Física La Plata (IFLP), CONICET
Calle 49 y 115, 1900
La Plata, Buenos Aires (Argentina)

[c] D. F. Coral, M. B. Fernández van Raap
Departamento de Física, Facultad de Ciencias Exactas
UNLP, Calle 49 y 115
1900 La Plata, Buenos Aires (Argentina)

[d] D. Muraca
Centro de Ciências Naturais e Humanas (CCNH)
Universidade Federal do ABC
Avenida dos Estados, 5001, Santa Terezinha
CEP 09210-580 Santo André-Sao Paulo (Brazil)

[e] D. C. Schinca, L. B. Scaffardi
Departamento de Ciencias Básicas, Facultad de Ingeniería
UNLP, Calle 1 y 47 (1900)
La Plata, Buenos Aires (Argentina)

Special Issue An invited contribution to a Special Issue on Nanoparticles with Lasers.

© 2017 Wiley-VCH Verlag GmbH & Co. KGaA, Weinheim

iron carbide. Depending on the solvent, NPs with different compositions and structures were observed. Wei et al.[22] synthesized Fe_3O_4 magnetic NPs by a coprecipitation method with sodium citrate and oleic acid as modifiers. FTIR analysis indicated that the modifier molecules were successfully conjugated with the surface of the magnetic NPs. Hysteresis curves showed saturation magnetization that decreases with increasing concentration of the surfactant. Maneeratanasarn et al.[23] synthesized iron NPs by nanosecond pulsed laser ablation of a bulk α-Fe_2O_3 target in water, acetone, and ethanol. They showed that it is possible to preclude the formation of iron metal in all three solvents by using a specific Fe oxide target, and better crystallinity was achieved in organic solvents.

Different laser–matter interaction mechanisms become dominant depending on the pulse-length range. In the nanosecond regime, the ablation mechanism is dominated by linear processes in which the energy of the laser pulse is absorbed on the surface of the metal. Heat conduction leads to a temperature rise that melts the material, evaporates it, and produces a plasma state due to melt expulsion. In the case of femtosecond laser pulses, the extreme intensities involved in the laser–matter interaction enhance nonlinear multiphoton absorption processes, by which pulse-energy transfer from the electron gas to the crystal is decoupled, since the latter requires about 10 ps, so that heat diffusion to the lattice is inhibited. Thermal phenomena may then be described by the so-called two-temperature model. The short interaction time produces a state of locally overheated liquid, which, due to the extreme pressures and temperatures occurring during interaction, expands rapidly as a mixture of liquid droplets and vapor in a process known as phase explosion. These different processes eventually lead to the formation of self-organized spherical nanostructures with different morphological, structural, compositional, and size characteristics compared with those generated in the nanosecond regime.

Herein, we report the optical, magnetic, and structural characteristics of colloids produced by ultrashort pulse laser ablation (UPLA) of a solid Fe target immersed in four different solvents: HPLC water, an aqueous solution of trisodium citrate (TSC), acetone, and ethanol. The suspensions were analyzed by optical extinction spectroscopy (OES), vibrating-sample magnetometry (VSM), micro-Raman spectroscopy, optical microscopy (OM), AFM, TEM, electron diffraction (ED), and small-angle X-ray scattering (SAXS) to assess NP shape, size distribution, magnetization, and composition. We also show that, under certain experimental conditions, submicrometer-sized iron oxide NP agglomerate in fractal patterns that show self-similar properties. Finally, self-assembled annular structures on the nanometer scale were observed and are reported for the first time.

Experimental Section

Colloidal suspensions of iron NPs in different media were fabricated by femtosecond pulse laser ablation at different energies. A 10 mm-diameter and 1 mm-thick high-purity iron disk was used as the target. The disk was immersed in a vessel filled with 2 cm^3 of the used solvent, with a liquid column of 1 mm height over the target for obtaining high concentrated suspensions. A Ti:Sapphire system from Spectra Physics, emitting pulses of 120 fs with 1 kHz repetition rate centered at 800 nm wavelength, was used for laser ablation of the sample. A classical wave plate/polarizer system allows attenuation of the maximum output energy to 1 mJ per pulse. The laser beam was focused on the surface of the target disk with a lens of 5 cm focal length. Three laser pulse energies were used: 700, 300 and 70 μJ. An *XYZ* motorized micrometric stage allowed fine-focusing of the laser on the Fe disk and movement of the sample such that ablation took place at fresh surface points. The ablation process, which lasted 30 min for each laser energy, produced concentrated solutions that were dark greenish in water, dark reddish in TSC, dark greenish in acetone, and light green in ethanol. A schematic of the ablation process, together with the characterization techniques used in this work, is shown in Figure 1.

An NT-MDT Solver Pro microscope in semicontact mode with a scan rate of 1 Hz was used to record AFM images in air at room temperature. Topographical measurements were acquired by using rectangular-shaped cantilevers coated with Al on the reflex side. These cantilevers had a spring constant of 37–58 $N\,m^{-1}$ and pyramidal silicon nitride tips. APPNANO ACTA (6 nm curvature radius) and ACTA-SS (2 nm curvature radius) probes at a resonant frequency of 300 kHz were used for samples in each of the four solvents. AFM provides a three-dimensional surface profile. Lateral dimensions are distorted by tip–sample convolution effects. However, high *z* accuracy is obtained when height measurements with a minimum scanning vertical step of 0.012 nm are recorded. For these measurements, part of the as-prepared colloidal suspension was sonicated and diluted to 1/100 (v/v) for each of the above-mentioned solvents. A drop of such a diluted sample was placed on a freshly cleaved muscovite mica sheet (V-1 grade, SPI Supplies) and dried for 12 h at room temperature. Analysis of the mica sheet indicated an average roughness of 0.0612 nm.

Magnetization *M* as a function of magnetic field was measured at room temperature by using a VSM Lake Shore 7404 vibrating-sample magnetometer operated at a maximum applied field of $\mu_0 H_{max} = 1.9$ T (equivalent to $H_{max} = 19$ kOe). Magnetic measurements were performed on 50 μL of colloidal suspension sealed in a heat-shrinkable tube to prevent sample evaporation and spills. The data were normalized by Fe mass concentration, which was measured by weighing the solid target before and after ablation. The difference was then divided by the total volume to obtain the mass concentration of Fe.

A TEM-MSC (JEOL 2100, acceleration voltage 200 KV) was used for electron microscopy imaging and ED analysis. The as-prepared suspensions of Fe NPs in the different solvents were appropriately diluted and sonicated for 15 min, and a drop of each was deposited and dried on a carbon-coated copper grid, followed by plasma cleaning to avoid possible organic residues. Images on a single-tilt sample holder were captured with a TV Gatan ES500W and a CCD (TVips-16MP) camera.

SAXS data were collected at the D01B-SAXS2 beam line with a Mar 165 CCD detector at a wavelength of $\lambda = 1.822$ Å ($\varepsilon = 6.804$ keV) after an Si (111) monochromator. For measurement, the as-prepared colloids were sonicated and injected between two clear ruby mica discs (25 μm thick each) of the liquid sample holder. The range of the momentum transfer vector $q = 4\pi\sin\theta/\lambda$ (where 2θ is the scattering angle), ranged from 0.06 to 3 nm^{-1}, and it was recorded with sample–detector distances of 975 and 1977 mm. Water was used as a secondary standard to express scattering in-

© 2017 Wiley-VCH Verlag GmbH & Co. KGaA, Weinheim

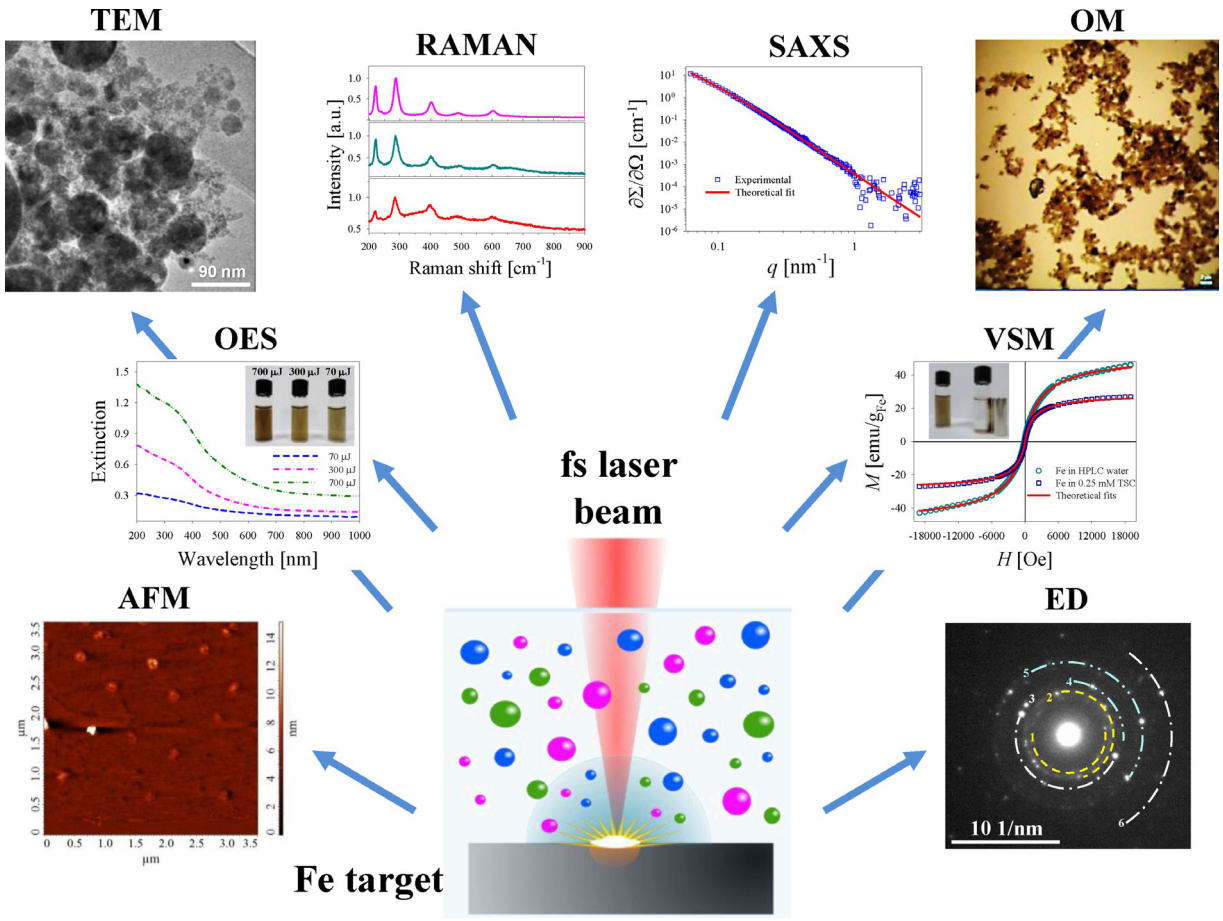

Figure 1. Schematic diagram depicting the fabrication of iron colloidal suspensions in liquids by femtosecond laser ablation together with different techniques used for characterization.

tensity on an absolute scale as differential cross section $\partial\Sigma/\partial\Omega$ [cm^{-1}] and to merge data from the two measurements. Raw data were corrected for absorption, background, and scattering due to solvent-density fluctuation prior to fitting.

A Shimadzu spectrophotometer (250–1100 nm wavelength range) was used for OES to measure the absorbance of colloidal suspensions of iron in different media immediately after fabrication to prevent possible NP coalescence.

Direct and inverted optical microscopes were used for OM observation of samples and micrometer-sized self-organized fractal structures. Raman spectra of the particles were measured with a Horiba-Jobin Yvon XPlora Plus confocal scanning microscope. A drop of iron colloid from a previously sonicated and diluted sample (1/10 v/v) was placed on a glass cover slide and dried in an oven with a temperature ramp from 25 to 50 °C over 15 min. The final temperature was then kept constant for 2 h.

2. Results and Discussion

2.1. Optical Extinction Spectroscopy

UV/Vis/NIR extinction spectra of Fe NP suspensions after UPLA at three different laser pulse energies in the four studied media are shown in Figure 2. For each solvent, the spectra for 700, 300, and 70 µJ are depicted. These show a general decrease in extinction with decreasing laser energy, indicating that, as may be expected, the amount of ablated material is smaller. This is also qualitatively supported by the overall decreasing coloration of the suspensions (insets to Figure 2). The UV/Vis/NIR extinction spectra of iron-based NP colloids lack the characteristic plasmon resonance typical of noble metals such as Au, Ag, and Cu, and this hinders the assessment of the presence of NPs in the suspensions from a spectroscopic point of view. Instead, monotonically decreasing spectra are observed in our experiments, except for a shoulder in the 300–400 nm range. From Mie calculations, these features are due to the presence of NPs with radii larger than 20 nm, which, although present in a small percentage, have a large enough cross section to be observable in the extinction spectra. Besides, for solvents containing carbon atoms (aqueous TSC, acetone, and ethanol), the formation of Fe_3C NPs, which have an absorption band in the 300–400 nm range, during the ablation process is highly probable due to the attachment of free carbon to Fe NPs at the plasma/liquid interface of the cavitation bubble in the laser-generated plasma plume. The efficiency of formation is dependent on the reactivity of the solvent with Fe atoms in the plasma plume.

In the case of ethanol, such a band is readily observed, since its reactivity with iron atoms at the high temperatures and

© 2017 Wiley-VCH Verlag GmbH & Co. KGaA, Weinheim

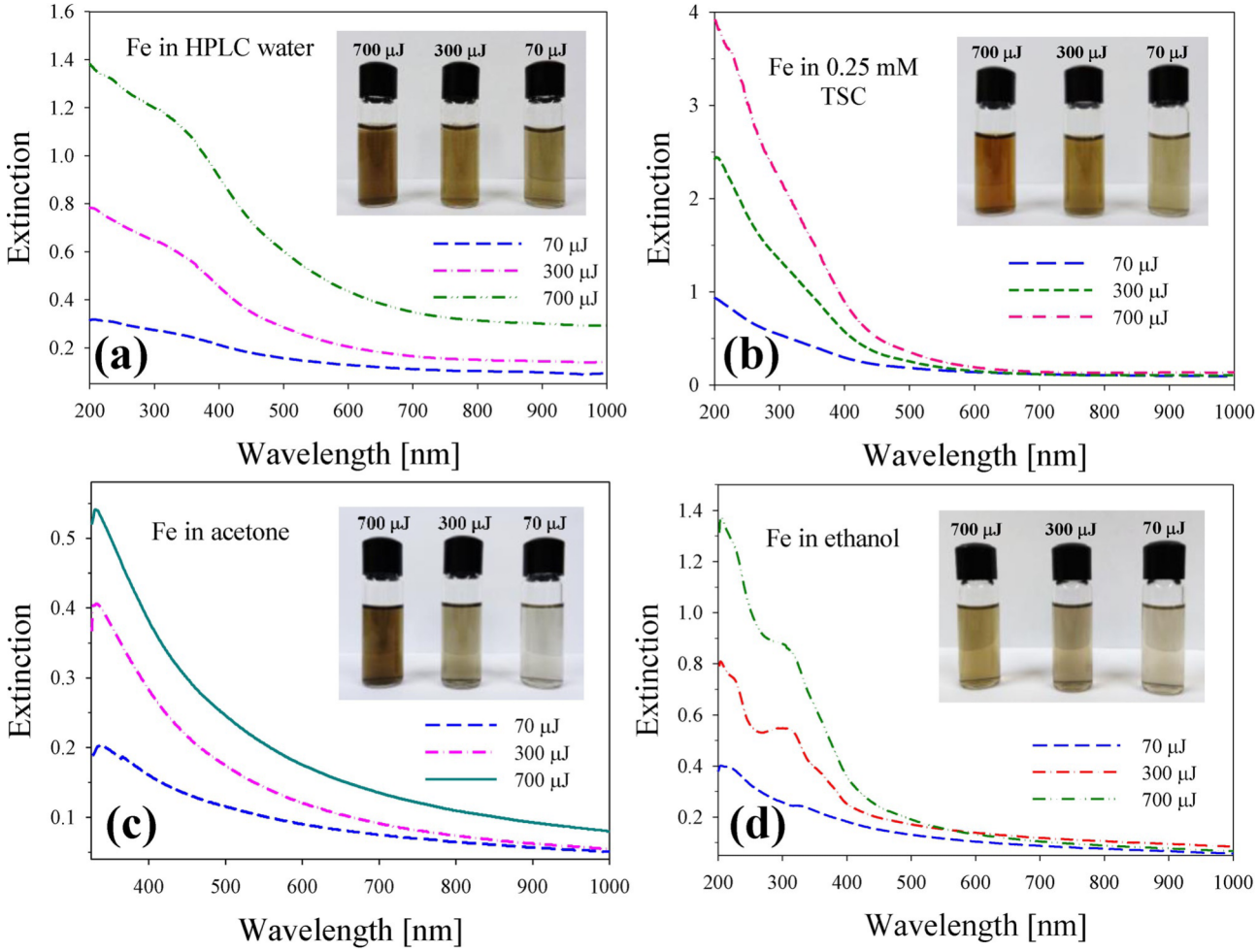

Figure 2. Extinction spectra of colloidal Fe NPs in a) HPLC water, b) aqueous TSC solution, c) acetone, and d) ethanol, obtained at three different pulse energies. For each medium, the inset shows vials arranged in decreasing energy from left to right. Extinction spectra for acetone in c) were very noisy for wavelengths shorter than 300 nm and are not shown.

densities encountered in the UPLA plasma plume is higher than those of the other organic solvents used in this work. Similar results were observed by other authors,[21] who, on the basis of the work of Khare et al.,[24] assigned the observed peak to the above-mentioned absorption band. In our experiments, this absorption band is weak for aqueous TSC and stronger for acetone. The lattice vibrational modes of single-crystal iron carbide have four modes, which are Raman-inactive. Hence, there is no information on the Raman spectrum of iron carbide in the literature.

Comparison of these spectra suggests that higher pulse energies produce colloids with more ablated material than those obtained at lower pulse energies. As can be deduced from spectroscopic data, the colloids are very similar in composition. So, in the rest of the paper, only the samples obtained with the maximum laser pulse energy (700 µJ) in HPLC water, aqueous TSC solution, acetone, and ethanol are discussed.

2.2. Fe in HPLC Water and Aqueous TSC Solution

2.2.1. Micro-Raman Spectroscopy

Figure 3 shows a 100× OM image of a drop of diluted iron colloid in HPLC water, in which a typical agglomeration pattern can be seen. Raman spectra were taken at different regions of this pattern and normalized to the maximum peak. The diameter of the laser spot at the sampling point is about the size of the scale bar, and the maximum power compatible with avoiding damage to the sample was used.

Although micro-Raman spectroscopy is a well-established and powerful technique for studying atomic and molecular bonds in chemistry and condensed-matter physics, care must be taken when it is applied to the study of iron oxides. Some authors reported possible size-induced phase transitions between α-Fe_2O_3 and γ-Fe_2O_3.[25] Further, focused lasers, as used in micro-Raman spectroscopy, may also induce structural changes in the sample, depending on the power used.[26] Excessive exposure of an iron oxide sample to laser radiation has been shown to generate hematite. The reported laser-power

© 2017 Wiley-VCH Verlag GmbH & Co. KGaA, Weinheim

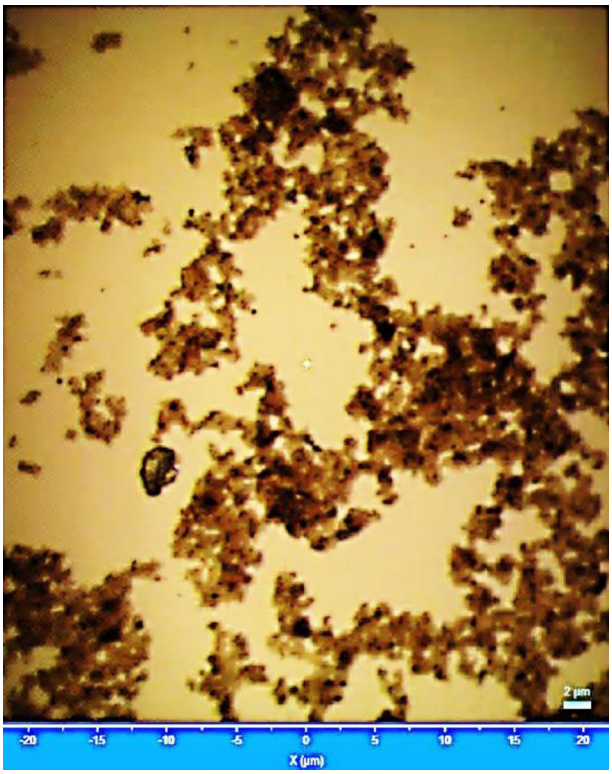

Figure 3. OM image of a diluted drop of iron colloid in HPLC water taken with a 100× objective. Scale bar is 2 µm.

thresholds for hematite formation differ widely, since they depend on experimental conditions such as wavelength, focusing objective, exposure time, and surface characteristics. Regarding this potential risk, a safe laser power that can be used for micro-Raman measurements on iron oxides is <0.8 mW. All our Raman spectra were recorded in this power regime with an exposure time of 10 s.

Figure 4 shows Raman spectra of iron colloid in HPLC water, recorded at three different regions of the sample. Depending on the location of the measurement spot, the Raman spectra exhibited Raman signals of magnetite (Fe_3O_4), maghemite (γ-Fe_2O_3), hematite (α-Fe_2O_3), or various mixtures thereof. The upper panel shows the Raman spectrum of a spot site at which only peaks corresponding to hematite were found. The lower panel is a spectrum showing peaks of hematite and maghemite, while the central panel shows peaks of hematite, maghemite, and magnetite coexisting in the same region of the sample.

Figure 5 shows the Raman spectra of other spot site, where only maghemite and magnetite were found (upper panel). At 660 cm^{-1}, the peaks for both oxides are superimposed. However, when the spectrum of pure maghemite[25] is subtracted from that shown in the upper panel, the spectrum of magnetite at 660 cm^{-1} is evidenced (lower panel).

Figure 6 shows the Raman spectrum of iron colloid in a 0.25 mM aqueous solution of TSC. The spectrum was taken

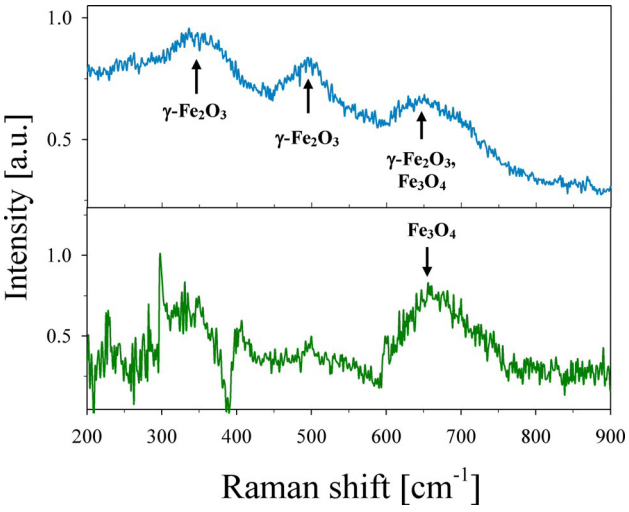

Figure 5. Raman spectrum of iron colloid in HPLC showing peaks corresponding to maghemite and magnetite (upper panel). Enhancement of magnetite peak at 660 cm^{-1} by subtraction of a pure maghemite spectrum (lower panel).

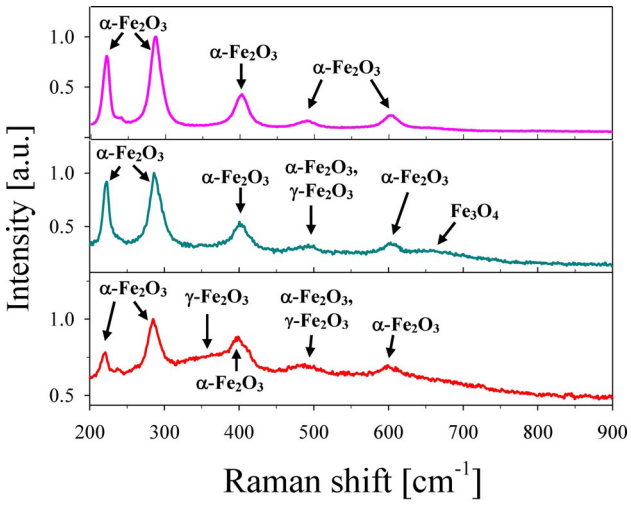

Figure 4. Raman spectra of iron colloids in HPLC water at different sample points. A mixture of iron oxide phases is observed.

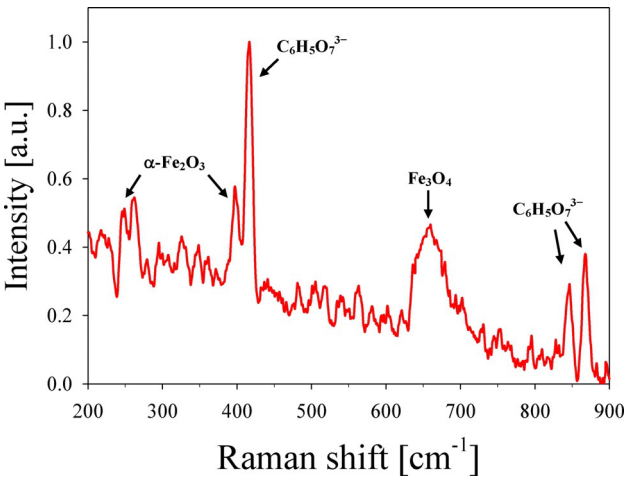

Figure 6. Raman spectrum of iron colloid in 0.25 mM aqueous TSC solution showing peaks corresponding to hematite, magnetite, and citrate.

© 2017 Wiley-VCH Verlag GmbH & Co. KGaA, Weinheim

with a laser power of 0.4 mW, below the phase-transition threshold. Raman peaks corresponding to magnetite, hematite, and citrate ($C_6H_5O_7^{3-}$) can be clearly seen.[27–29] This kind of spectrum shows that the samples are complex in structure, with different oxide phases in the same spot site. When Raman measurements were done on this kind of multiple-phase site with increasing laser power, only hematite Raman bands were finally observed, which suggests that a phase transition of the different magnetic oxides to laser-dependent nonmagnetic hematite was induced. However, laser-independent hematite-containing spot sites were also found in the same sample. This finding is similar to that reported by Chourpa et al.[26] for NPs synthesized by coprecipitation of ferrous and ferric salts.

2.2.2. TEM and ED

Figure 7 shows TEM images of dried iron colloids in different media. Figure 7a–d show NPs in HPLC water. Large NPs with a certain degree of agglomeration were selected for phase identification by selected-area electron diffraction. Although the images are not representative of the whole sample, spherical morphology of the particles is clearly observed. In general, NPs have radii smaller than 15 nm and coexist with some larger ones. Figure 7a shows an isolated NP, 30 nm in radius, surrounded by a thin layer, possibly of an iron hydroxide generated during laser ablation.[30] Figure 7b is a panoramic view showing the presence of different-sized NPs with indication of radii. Figure 7c is panoramic view that includes two core–shell NPs, indicated by dashed arrows. UPLA tends to produce hollow NPs,[16,31,32] as can be seen in the inset of Figure 7d. Figure 7e shows a central, 12 nm-radius, isolated Fe NP immersed in aqueous TSC together with some smaller ones in the range 2–3 nm. A group of typical-sized Fe NPs in ethanol is shown in Figure 7f. In the case of acetone, small NPs together with core–shell-type structures are observed (Figure 7g). Figure 7h shows Fe NPs in acetone forming self-assembled fractal-like aggregates. The inset shows an enlargement of part of the fractal assembly, in which a couple of core–shell NPs can be seen.

By using the same equipment, ED patterns were measured on selected NPs for phase identification. A typical pattern for an iron colloid in HPLC water is shown in Figure 8. The faint haloes suggest high crystallinity of the NPs. The ED pattern was indexed to the reflections of iron oxide (JCPDS cards #06-0696 for α-Fe, #75-0033 for Fe_3O_4, and #39-1346 for γ-Fe_2O_3). Crystallographic parameters of Fe_3O_4, γ-Fe_2O_3, and α-Fe were obtained by using electron microscopy simulation software (JEMS).[33] Table 1 lists the electron diffraction rings according to the interplanar distances $d_{\alpha-Fe}$, $d_{Fe_2O_3}$, and $d_{Fe_3O_4}$ and the corresponding Miller indices *h*, *k*, and *l*. No reflections characteristic of other structures appear. Iron oxide phases corresponding to magnetite (Fe_3O_4), ferric oxide (Fe_2O_3), and α-Fe can be observed for different interplanar distances.

Table 1. Crystallographic parameters derived from the electron diffraction pattern of iron colloid in HPLC water.

Ring	$d_{\alpha-Fe}$ [nm]	$d_{Fe_2O_3}$ [nm]	$d_{Fe_3O_4}$ [nm]	(*h*, *k*, *l*)
1			0.299	(0, 2, 2)
2			0.255	(1, 3, 3)
3	0.201			(0, 1, 1)
4		0.184		(0, 2, 4)
5		0.147		(3, 0, 0)
6	0.102			(0, 2, 2)

2.2.3. Atomic Force Microscopy

AFM images of colloidal Fe NPs in HPLC water are shown in Figure 9. Figure 9a is a 50×50 μm panoramic image of an appropriately diluted sample of a freshly prepared colloid, in which numerous isolated NPs can be seen as small dots. The color scale represents the height (diameter) of the particles. Dashed lines drawn over selected NPs correspond to the height profiles shown in Figure 9c, which shows that the typical radius is less than 5 nm. A more detailed size histogram, in which more than 400 NPs were taken into account, is shown in Figure 9d. A log-normal curve with modal radius of 1.8 nm can be fitted to the histogram bars. Figure 9b is a 3×3 μm close-up of Figure 9a, in which isolated NPs 1 and 1.25 nm in radius are shown (inset with height profiles).

Figure 10 shows AFM images of colloidal Fe NPs in a 0.25 mM aqueous solution of TSC. Figure 10a is a 15×15 μm panoramic image of an appropriately diluted sample of a freshly prepared colloid showing isolated NPs. The vertical color scale represents the height (diameter) of the particles. Height profiles of selected NPs in Figure 10a are shown in Figure 10c. The size histogram in Figure 10d can be fitted by a log-normal size distribution with modal radius of about 2 nm. Figure 10b is a 2×2 μm AFM image of another region of the sample showing isolated NPs of about 2.5 nm radius (inset).

The AFM results for water and aqueous TSC solution show log-normal size distributions with similar modal radii close to 2 nm, while the latter has a broader size distribution than the former.

2.2.4. Small-Angle X-ray Scattering

Figure 11 shows a log–log plot of the scattering differential cross section $d\Sigma/d\Omega$ against scattering vector *q* for colloidal Fe NPs dispersed in HPLC water. For large *q* values, a linear behavior with slope of −4 is observed, consistent with the Porod scattering law for spherical particles. On the other hand, for small *q* values, the curve tends to a constant $d\Sigma/d\Omega$ value consistent with the Guinier law for polydisperse NPs.

To obtain morphological and size information from the overall scattering curve, a model based on the scattering of polydisperse spherical particles was considered [Eq. (1)]:

$$\frac{d\Sigma}{d\Omega} = N_p \int_0^\infty \left[3\Delta\eta V \frac{\sin(qr) - \boldsymbol{qr}\cos(qr)}{(qr)^3}\right]^2 g(r)dr \qquad (1)$$

where N_p is the particle density, $\Delta\eta$ the scattering-length density difference between particle and water, *V* the volume of a particle of radius *r*, and $g(r)$ the size log-normal distribution

© 2017 Wiley-VCH Verlag GmbH & Co. KGaA, Weinheim

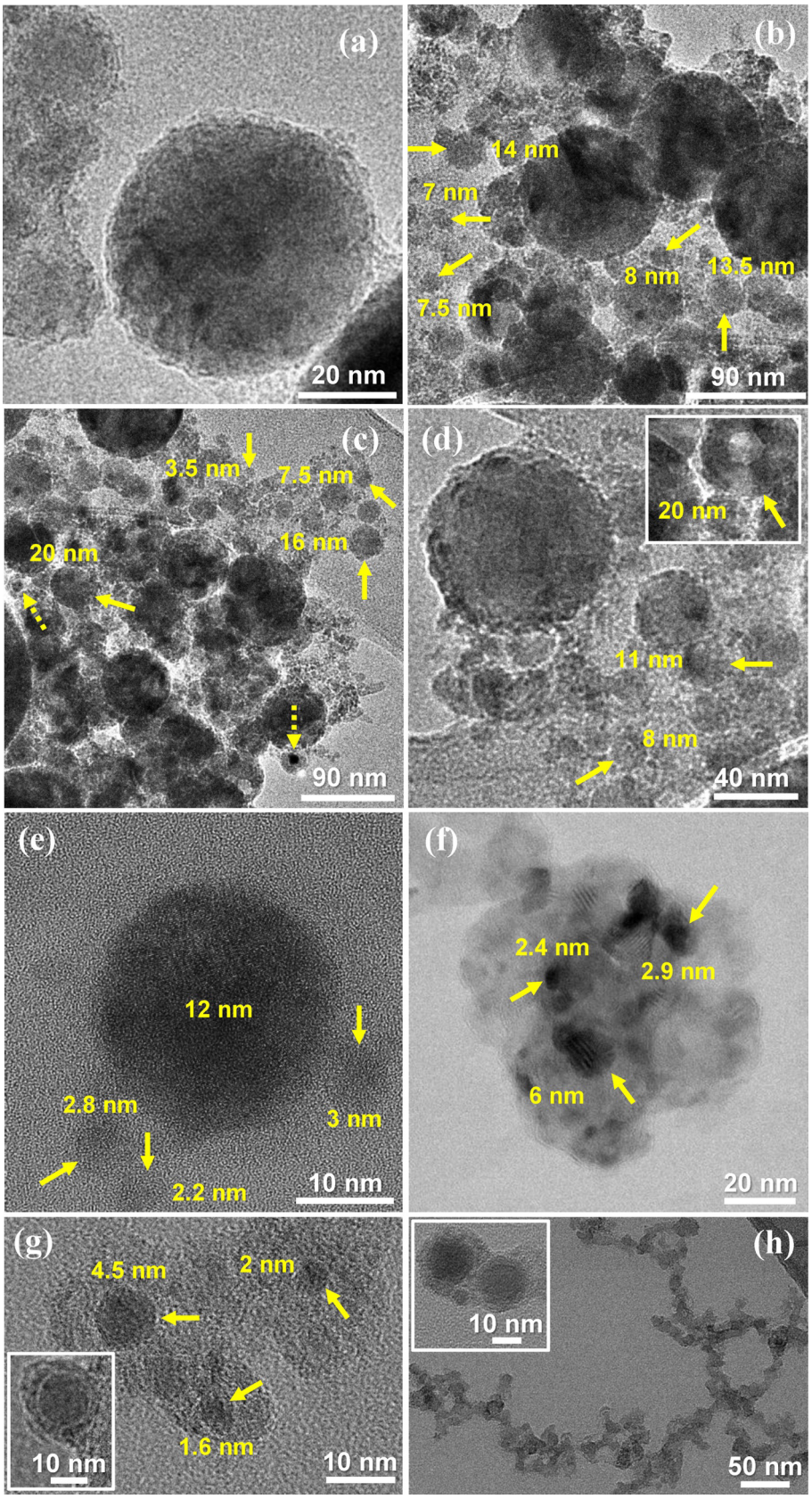

Figure 7. TEM images of iron NPs by femtosecond laser ablation in different media. a)–d). Fe NPs in HPLC water showing spherical shape and sizes. Numbers indicate the NP radii. Core–shell NPs are indicated by dashed arrows in c), and a hollow NP is shown in the inset of d). e) Isolated Fe NPs in aqueous TSC solution with small (2–3 nm) and larger (12 nm) radii. f) A group of typical-sized Fe NPs in ethanol. g) Small Fe NPs produced in acetone, among which core–shell NPs can be seen (inset). h) Fe NPs in acetone showing self-assembled fractal-like aggregation. The inset shows a couple of core–shell NPs within the fractal assemble.

© 2017 Wiley-VCH Verlag GmbH & Co. KGaA, Weinheim

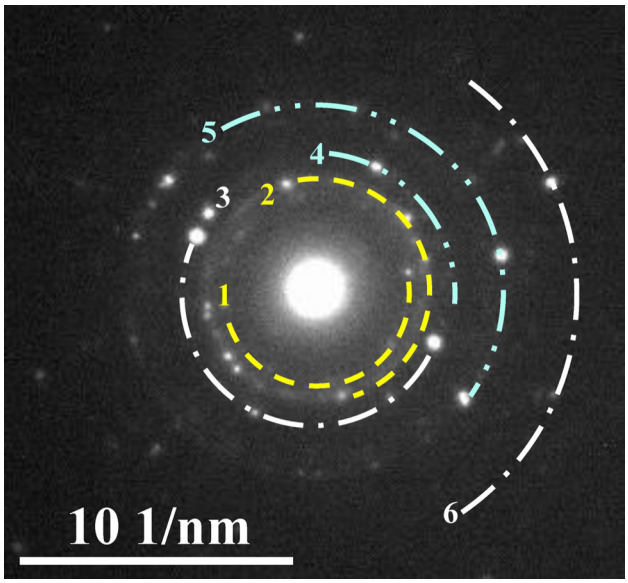

Figure 8. ED pattern for iron colloid in HPLC water. Labeling of the rings is according to the increasing values of the scattering vector *q*.

of median r_0 and standard deviation σ. Fitting of the experimental data (empty squares in Figure 11) with $\Delta\eta N_p^{1/2}$, r_0, and σ as fitting parameters yielded $r_0 = 1.59 \pm 0.03$ nm and $\sigma = 0.914 \pm 0.003$, which correspond to mean particle radius $\langle r \rangle = r_0 e^{\sigma^2/2} = 2.4 \pm 0.1$ nm. The size distribution shown in the inset of Figure 11 is in good agreement with that from AFM analysis shown in Figure 9d.

2.2.5. Magnetic Properties

Comparative field-dependent dc magnetization curves at room temperature for Fe colloids in HPLC water and a 0.25 mM aqueous solution of TSC after subtraction of the diamagnetic contribution of water are shown in Figure 12. The loops display the shape commonly observed for an assembly of magnetic NPs with randomly oriented magnetic-anisotropy axes.

The small area inside the hysteresis loop indicates that coercivity and remanent magnetization (see inset in the upper left quadrant of Figure 12) are less than 60 Oe and 1 emu g_{Fe}^{-1}, respectively, which suggest single-domain MNPs. This is in agree-

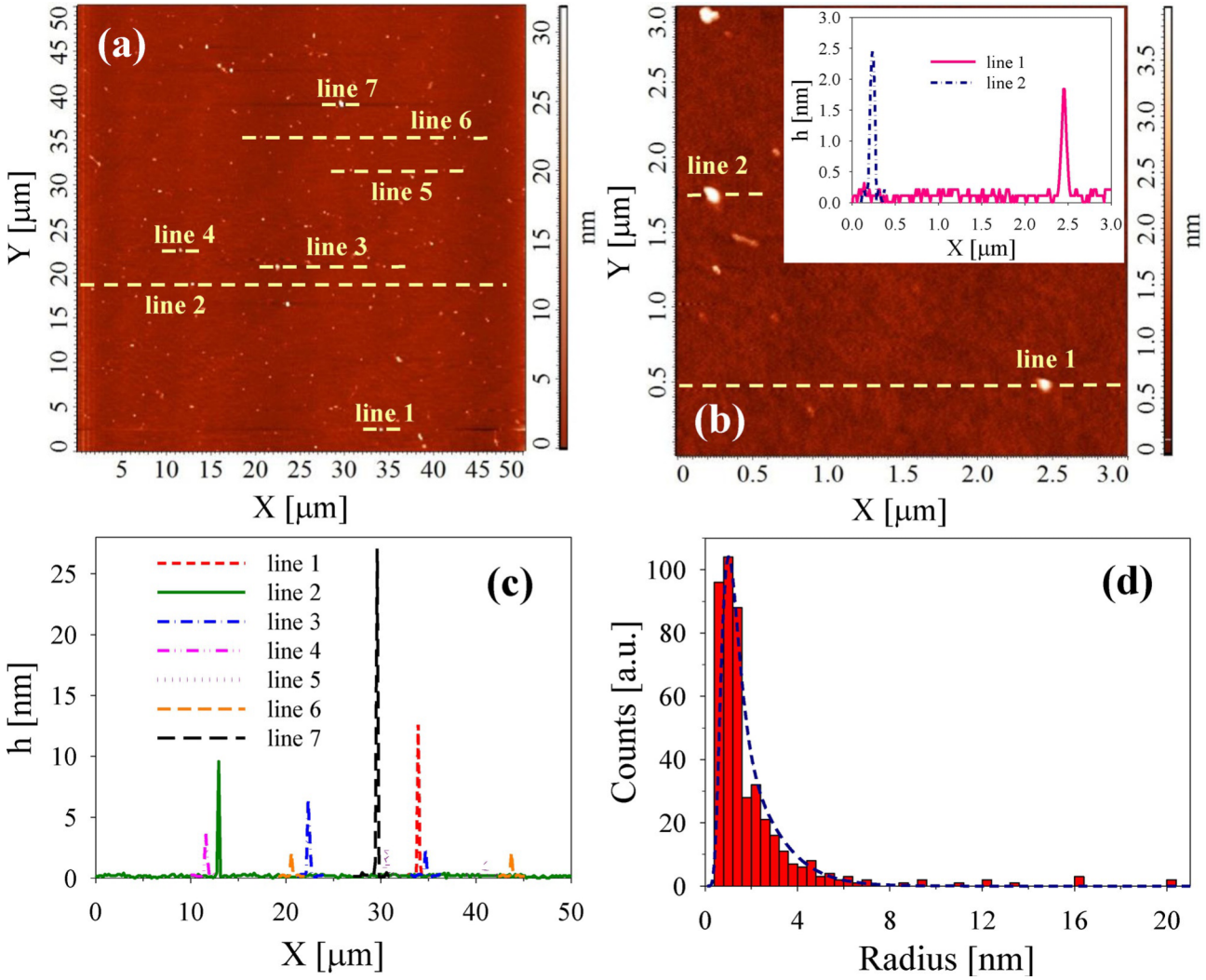

Figure 9. AFM images and size analysis of iron colloid NPs obtained by laser ablation in HPLC water. a) 50×50 μm panoramic image of isolated single NPs. b) 3×3 μm image of a) showing typical sizes of small spherical NPs. The inset shows height profiles of two selected lines. c) Height profiles of selected lines 1–7 of a) showing typical diameters of NPs. d) Radius histogram together with a log-normal fitting curve with modal radius of 1.8 nm.

© 2017 Wiley-VCH Verlag GmbH & Co. KGaA, Weinheim

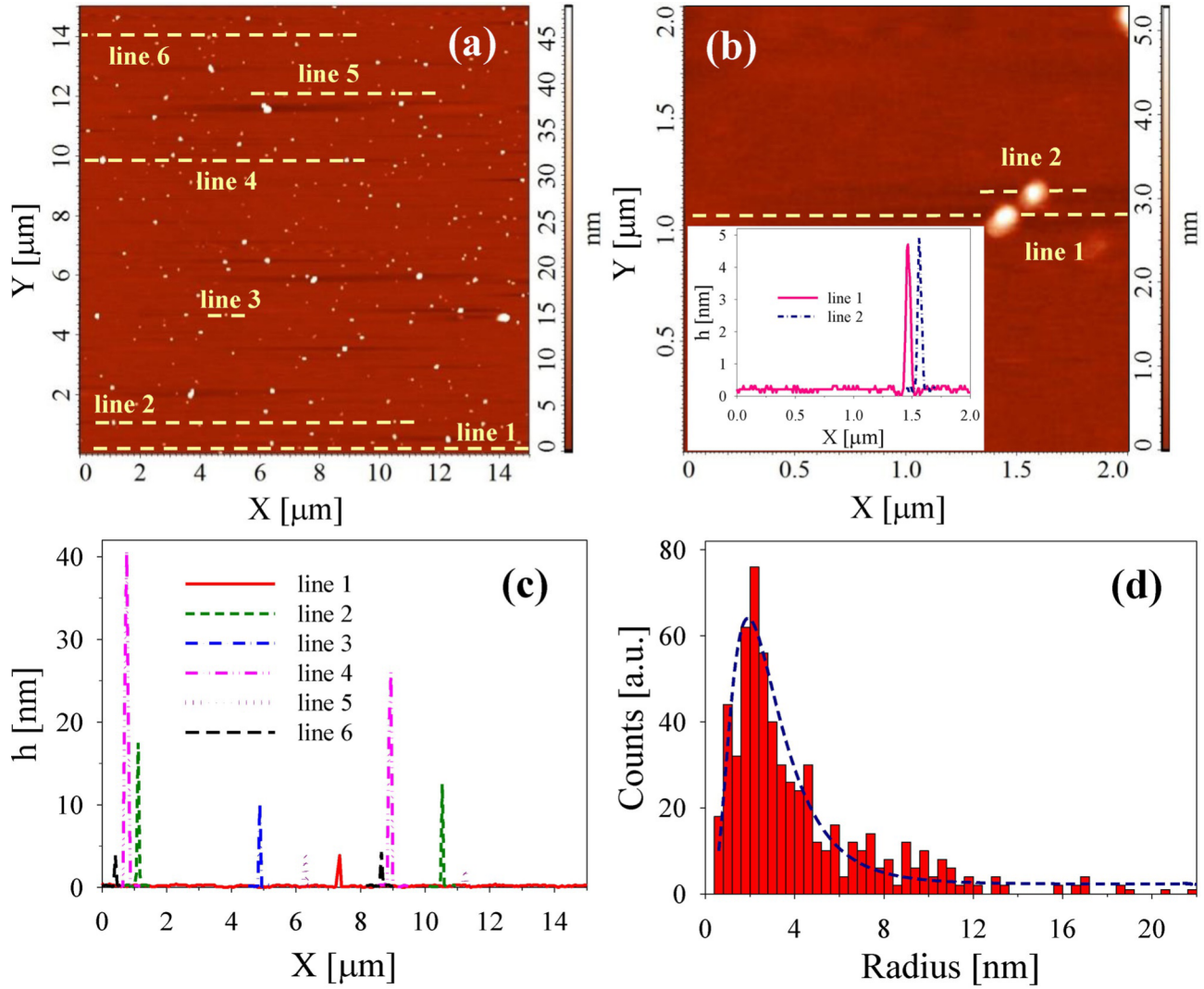

Figure 10. AFM images and size analysis of iron colloid NPs obtained by laser ablation in 0.25 aqueous TSC solution. a) 15×15 μm panoramic image of isolated single NPs. b) 2×2 μm image showing small spherical NPs together with their height profiles (inset). c) Height profiles of selected lines 1–6 in a) showing typical NPs diameter. d) Radius histogram together with a log-normal curve fitting the histogram bars.

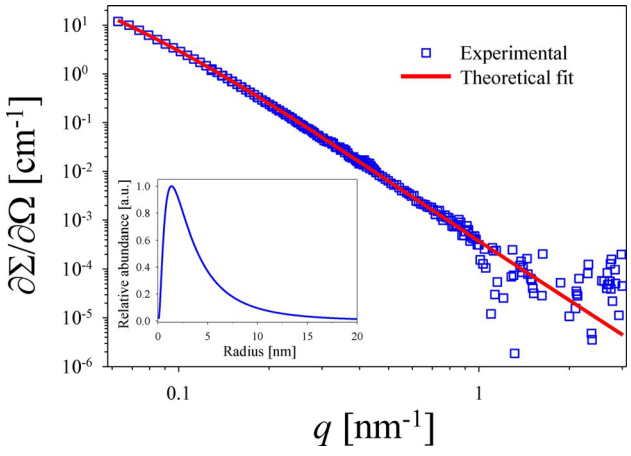

Figure 11. Experimental (empty squares) and theoretical fit (full line) of SAXS measurements on iron colloids in HLPC water. The inset shows the fitted size distribution.

ment with colloidal superparamagnetic behavior, which was verified by fitting data with a Langevin function, weighted with a log-normal distribution of magnetic moment $g(\mu)$ and a linear contribution proportional to the high-field susceptibility χ_p [Eq. (2)]:

$$M(H) = N\int_0^\infty \mu\left[\coth\left(\frac{\mu\mu_0 H}{k_B T}\right) - \frac{k_B T}{\mu\mu_0 H}\right] g(\mu)d\mu + \chi_p H \qquad (2)$$

The mean magnetic moment $\langle\mu\rangle$ was retrieved from log-normal fitted parameters (median μ_0 and dispersion σ of the variable lnμ) with $\langle\mu\rangle = \mu_0 e^{\sigma^2/2}$, while saturation magnetization is given by $M_S = N\langle\mu\rangle$, where N is the particle number density. Table 2 lists results for M_S, $\langle\mu\rangle$, N, magnetic radius r_M, and total radius r_T of colloidal Fe NPs derived from the VSM measurements in water and aqueous TSC solution.

From the Langevin fit of magnetization curves, log-normal size distributions can also be retrieved by considering that each particle of volume V is magnetized on saturation as

© 2017 Wiley-VCH Verlag GmbH & Co. KGaA, Weinheim

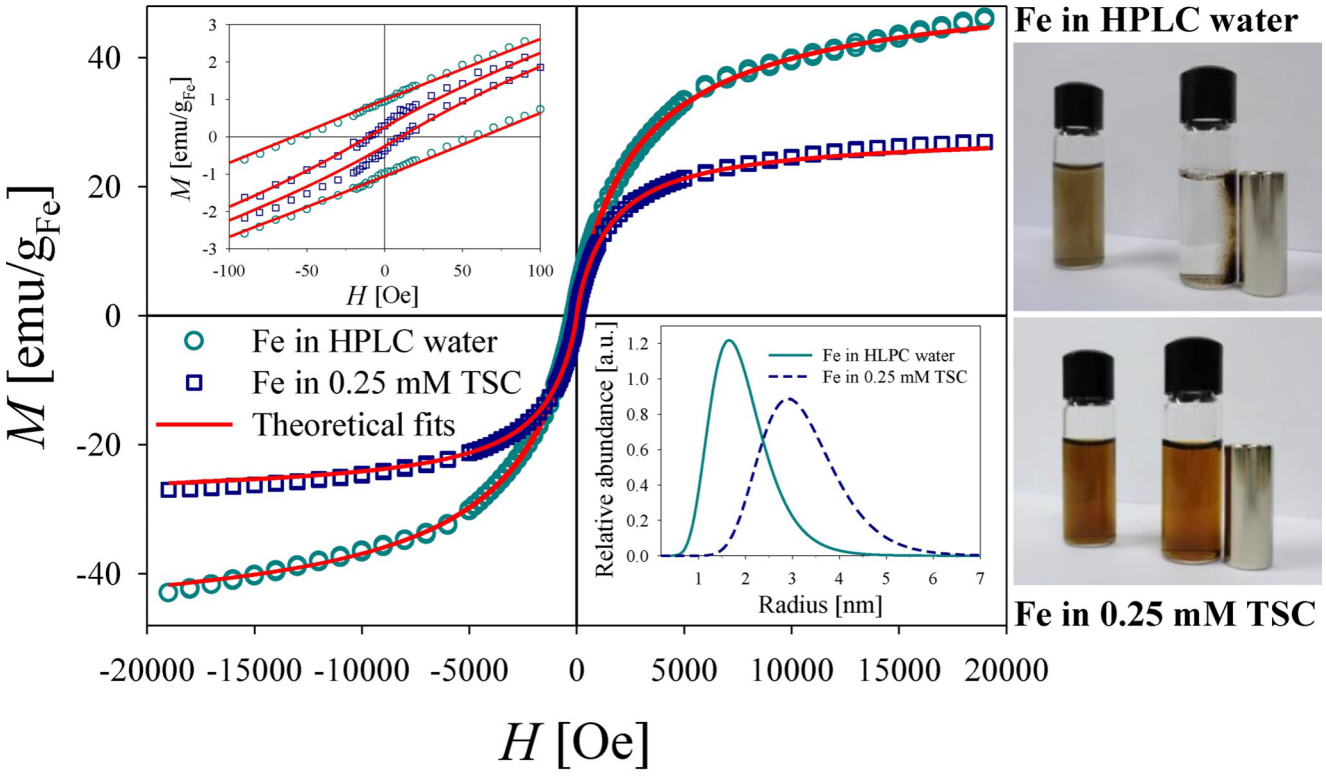

Figure 12. Magnetization curves for as-prepared iron colloid in HPLC water and aqueous TSC obtained by laser ablation with 700 μJ pulse energy. The insets show an enlargement of the very small area of the hysteresis cycle at the origin (upper left) and the NP size distribution derived from curve fitting (lower right). Right: photographs of vials illustrating the magnetic force effect on the NPs of a NdFeB magnet.

Table 2. Saturation magnetization M_S, magnetic moment $\langle\mu\rangle$, number density N, magnetic radius r_M, and total radius r_T of colloidal Fe NPs, derived from VSM measurements in water and aqueous TSC solution.

	Fe in HPLC water	Fe in 0.25 mM TSC
M_S [emu g_{Fe}^{-1}]	49.3 ± 0.7	26.7 ± 0.2
$\langle\mu\rangle$ [μ_B]	1606 ± 21	3468 ± 28
N [g^{-1}]	2.9×10^{18}	0.7×10^{18}
r_M [nm]	1.1 ± 0.4	1.5 ± 0.4
r_T [nm]	1.9 ± 0.6	3.2 ± 0.9

$M_S = {}^{\langle\mu\rangle}/_{V}$. Besides, r_M and r_T can be calculated by considering the experimental and theoretical magnetization, respectively. The difference between the total and magnetic radii gives the thickness of the frustrated magnetic layer. Log-normal radius distributions centered at 1.7 nm for HPLC water and at 3 nm for aqueous TSC were obtained (see inset in the lower right quadrant of Figure 12). These results are in good agreement with the size distributions obtained by AFM measurements.

Although the raw data show a diamagnetic component ($\chi_p < 0$), subtracting this contribution reveals that no saturation is reached even at 19 kOe, possibly due to NP surface effects (frustrated magnetic layer or organic coating). This effect is clearly observed in Figure 12 and also in the data of Table 2, where it can be seen that the mean magnetic moment and magnetic saturation of the particles are higher for Fe NPs in HPLC water without any coating (49.3 emu g_{Fe}^{-1}) than for Fe NPs in aqueous TSC (26.7 emu g_{Fe}^{-1}). This supports the idea that TSC acts as a surface modifier, decreasing the saturation magnetization by a surface spin disorder effect. In both cases, M_S is much smaller than that of bulk Fe (217 emu g_{Fe}^{-1}).[34]

The smooth change in magnetization slope in the region near zero applied field (inset in the upper left quadrant) evidences that different oxide phases could be present. Considering that particles in that this range should be in the superparamagnetic regime, the observed values of remanence and coercive field could be attributed to a spin surface effect or weak interface effect between two magnetic phases.

Migration of the NPs in HPLC water towards a NdFeB magnet placed very close to the vial is a visual indication of their magnetic properties (photograph in Figure 12). However, in the case of magnetic NPs in aqueous TSC, no migration is observed, even after several hours of magnet–vial interaction. This is likely due to the electrically repulsive sheath that TSC forms around each NP.

Our results on the magnetization properties of iron colloids agree with those reported by Wei et al.[22] for Fe_3O_4 NPs synthesized by coprecipitation with TSC and oleic acid. However, Maneeratanasarn et al.,[23] who reported on the synthesis of magnetic NPs by laser ablation of a bulk α-Fe_2O_3 target in ethanol, deionized water, and acetone, found hysteresis curves with non-negligible area and much lower saturation magnetization than in our case.

© 2017 Wiley-VCH Verlag GmbH & Co. KGaA, Weinheim

2.3. Iron Colloids in Acetone and Ethanol

2.3.1. Micro-Raman Spectroscopy

Figure 13 shows Raman spectra of an iron colloid in acetone at two different regions of the sample. The upper panel corresponds to a spot site with only hematite Raman signals, while the lower panel shows mixed signals of hematite and magnetite from another site.

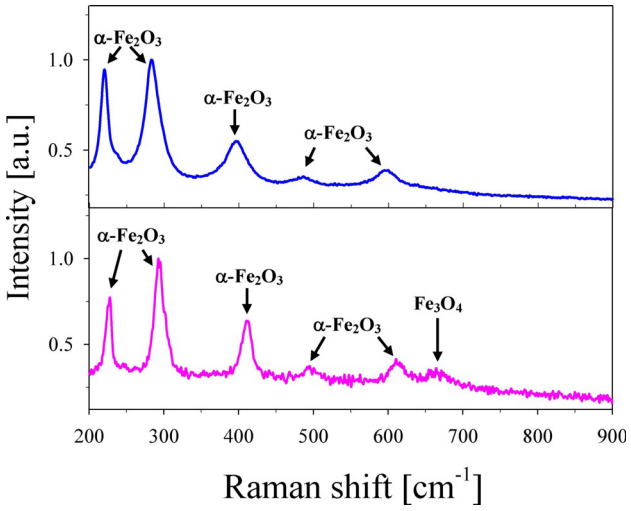

Figure 13. Raman spectra of iron colloid in acetone at two different regions of the sample. The upper panel shows only Raman signals of hematite, while the lower panel shows mixed signals of hematite and magnetite.

In the case of ethanol, results similar to those for acetone were obtained. The Raman spectra shown in Figure 14 correspond to two different sample spot sites: in one of them, only Raman signals of hematite were observed (upper panel), while the other shows mixed signals of hematite and magnetite.

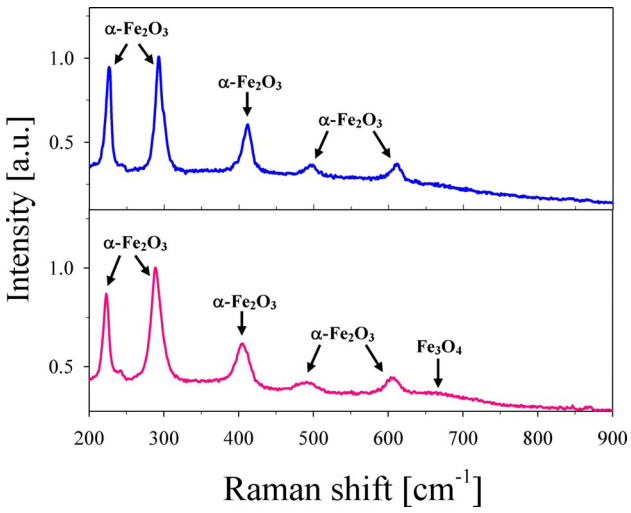

Figure 14. Raman spectra of iron colloid in ethanol at two different regions of the sample. The upper panel shows only Raman signals of hematite, while the lower panel shows mixed signals of hematite and magnetite.

Micro-Raman spectra of samples freshly prepared by UPLA in the four solvents show the presence of magnetite, hematite, and maghemite. These results differ from those presented by Amendola et al.,[20] who reported only magnetite for nanosecond PLA in water.

2.3.2. Atomic Force Microscopy

Figure 15 shows AFM images of colloidal Fe NPs obtained for a 1/100 (v/v) diluted sample in acetone. Figure 15a is a 55× 55 μm panoramic view showing isolated spherical NPs of typical sizes. Selected NPs are indicated by lines 1–4, the height profiles (diameters) of which are shown in Figure 15c according to the vertical color scale. Figure 15b is a 4×4 μm close-up view of another region of the sample showing three isolated NPs of 4, 6, and 9 nm radius. Figure 15d is a size histogram for about 400 NPs in different regions of the sample, showing a modal radius of about 4 nm and a very wide size distribution.

Figure 16 shows AFM images of colloidal Fe NPs obtained with a 1/100 (v/v) diluted sample in ethanol. This solvent has a smaller surface tension compared with water, with less interaction with the mica surface, so that the boundary of the drop expands faster. This means that dewetting processes at the drop boundary may form characteristic fingerlike patterns, as shown in Figure 16a, and thus a large number of NPs are collected in the resulting branches. Particles can be observed in isolated form or in agglomerates produced in the drying process of the sample. Some of the isolated particles are indicated by lines 1 to 6, the height profiles (diameters) of which are shown in Figure 16c according to the vertical color scale. The selected particles have radii in the range 1–5 nm. A more detailed statistics over hundreds of particles yielded the size distribution histogram shown in Figure 16d, together with its lognormal fitting curve, showing a modal radius of 4 nm and a dispersion including NPs up to 10 nm. A typical NP agglomerate is shown in Figure 16b, together with cross-sectional profiles along the directions indicated by lines 1 and 2. The profile curves (inset) suggest that this agglomerate is formed by three particles along line 1 and by two particles along line 2.

Comparison of the AFM histograms for suspensions obtained in acetone and ethanol indicates that the modal radius for both is almost the same, but the size dispersion is much larger in the former solvent than in the latter.

2.3.3. Magnetic Properties

Magnetization curves for samples in acetone and ethanol are shown in Figure 17. In this case, saturation magnetization values for both media are quite similar (30.8 and 26.5 emu g_{Fe}^{-1}, respectively). The photographs in Figure 17 show NP migration, within a few seconds, towards an external NdFeB magnet. One of the most striking features of this analysis is the almost zero hysteresis-cycle area of the *M* versus *H* plot (upper left inset). These characteristics support the idea that the obtained NPs are single-domain particles with a relatively high magnetization at high external fields.

© 2017 Wiley-VCH Verlag GmbH & Co. KGaA, Weinheim

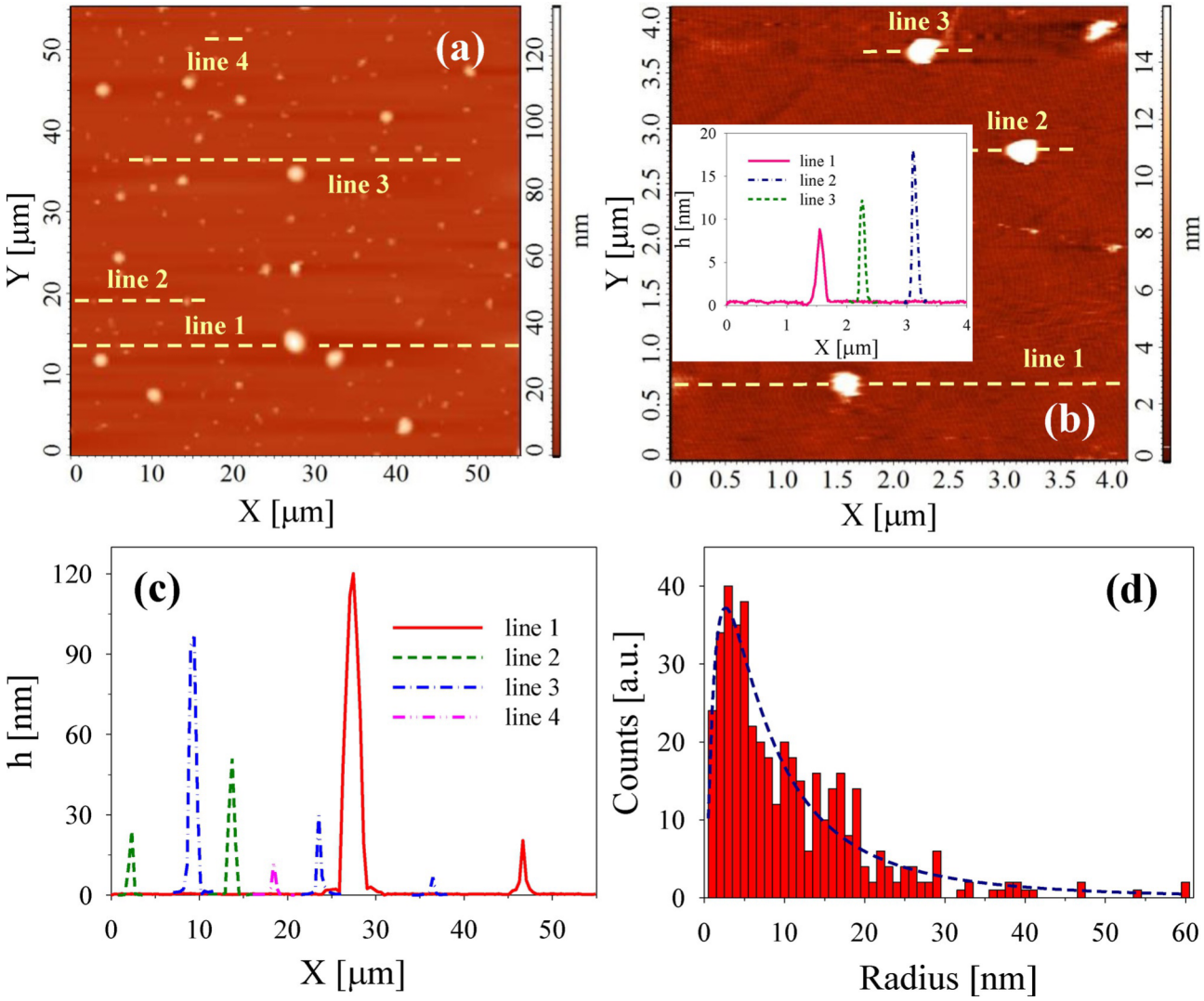

Figure 15. AFM size analysis of the obtained colloidal Fe NPs obtained by laser ablation in acetone. a) 55×55 μm panoramic image of isolated single NPs. b) 4×4 μm image showing small spherical NPs together with their height profiles (inset). c) Height profiles of selected lines 1–4 in a) showing typical NP diameter. d) Radius histogram together with a log-normal curve fitting the histogram bars.

For this kind of sample, a second magnetic contribution is needed to fit the overall range of H, which may be written as a Langevin function representing the superparamagnetic contribution of larger magnetic NPs, yielding in this way a bimodal size distribution. Thus, the full expression for the VSM fit is described by Equation (3):

$$M(H) = N_1 \int_0^\infty \mu_1 L\left(\frac{\mu_1 \mu_0 H}{k_B T}\right) g(\mu_1) d\mu_1 + N_2 \int_0^\infty \mu_2 L\left(\frac{\mu_2 \mu_0 H}{k_B T}\right) g(\mu_2) d\mu_2 + \chi_p H \quad (3)$$

Best-fit parameters for the bimodal log-normal distribution are listed in Table 3 and labeled as 1 or 2 for each contribution.

Comparing magnetization curves for Fe magnetic NPs dispersed in organic solvents with those for Fe magnetic NPs dispersed in water reveals a lower high-field susceptibility of the former, which indicates that the surface effects are minimized in the NPs dispersed in organic solvents, which is also consistent with larger NPs. In both cases, the fraction of small particles (4.1 and 5.2 nm for Fe magnetic NPs dispersed in ethanol and acetone, respectively) is smaller than the fraction of larger NPs. Size distributions derived from VSM analysis (inset in lower right quadrant in Figure 17) are in very good agreement with those derived from AFM measurements.

2.4. Self-Organized Structures of Iron Colloids in HPLC Water

Self-organization of NPs was observed at different size scales with appropriate microscopes. Figure 18 shows optical micrographs of a drop of iron colloid in HPLC water, sonicated for 15 min, diluted to 1/10 (v/v) from the as-prepared laser-ablation sample, and dried by increasing the temperature from 25 to 50 °C over 15 min. In this process, the deposited drop un-

© 2017 Wiley-VCH Verlag GmbH & Co. KGaA, Weinheim

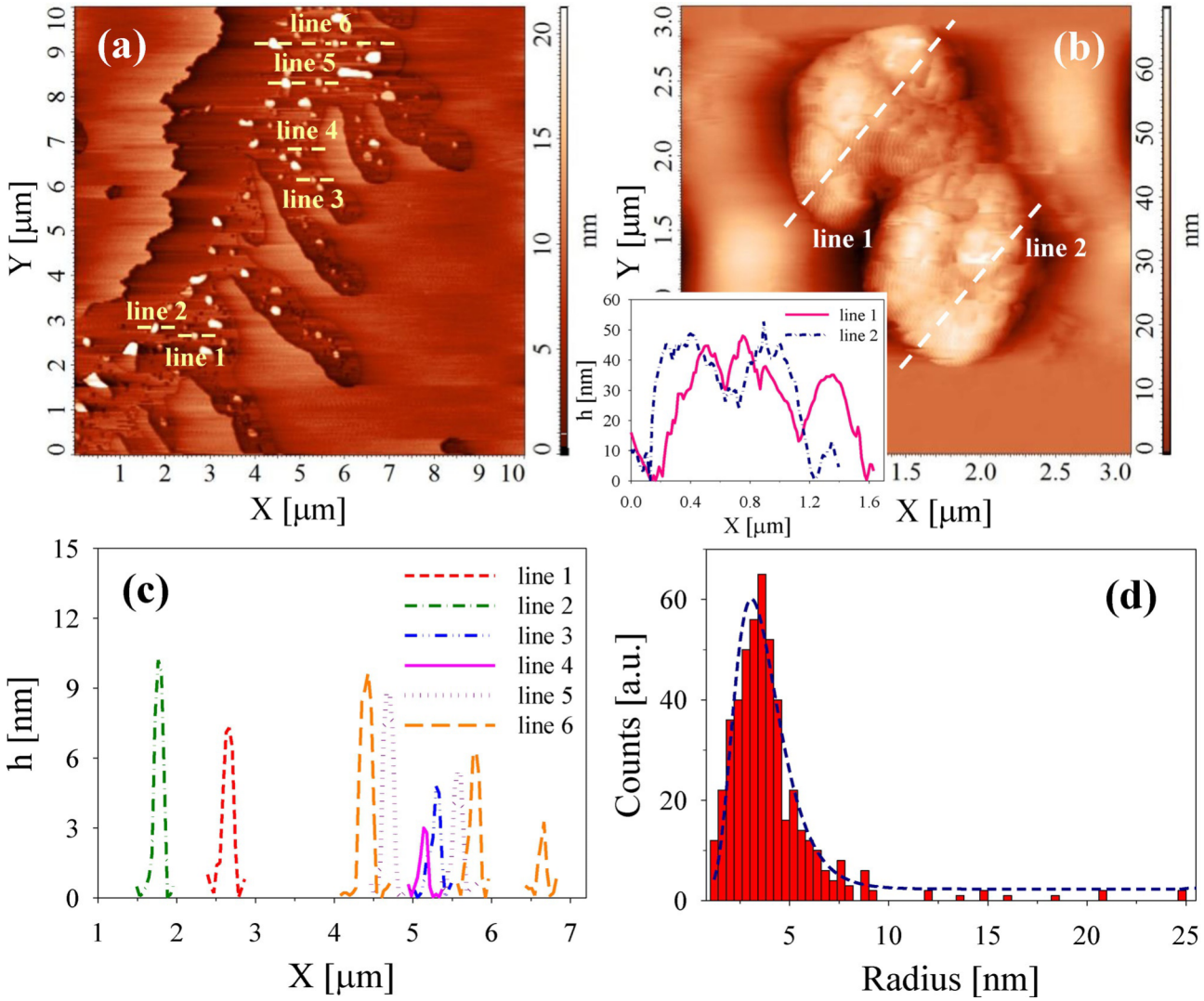

Figure 16. AFM size analysis of colloidal Fe NPs in ethanol. a) 10×10 μm panoramic image of isolated single NPs and agglomerates. b) 3×3 μm image showing a single agglomerate formed by several NPs. c) Height profiles of selected lines 1–6 in a) showing typical NP diameter. d) Radius histogram together with a log-normal curve fitting the histogram bars.

dergoes evaporation with fast temperature rise, which induces nonequilibrium conditions. Diffusion of NPs inside the drop during drying contributes to the formation of the observed 2D fractal structures. Thus, the resulting structure depends on the colloid concentration and on the initial temperature gradient of the drying process. The drying protocol mentioned above was similar to that used in a previous work on Ag NPs formed by UPLA in water,[31] to enhance the possible development of fractal-like structures. Figure 18a and b show self-agglomeration preferentially at the center zone of the dried drop. At size scales differing by one order of magnitude (20 and 2 μm in Figure 18a and b, respectively) and even three orders of magnitude (TEM image in Figure 7h), the auto-similar nature of the pattern is evident. These micrometer-sized particles agglomerate in patterns compatible with the topographic characteristics of 2D percolation cluster fractals.[35] The inset in Figure 18a shows the simulation of a percolation cluster of fractal dimension 1.89, the general pattern of which agrees with the observed experimental fractal. These kinds of samples are those used for the Raman analysis described in Sections 2.3 and 3.3.

Figure 18c and d also show another type of fractals, located preferentially close to the boundary of the dried drop. This kind of ramified growth is typical of a diffusion-limited aggregation (DLA) process, applicable to any particle system in which diffusion (Brownian motion) is the primary means of transport.[36] Its 2D fractal dimension is 1.70. The greenish and reddish colorations in the branches of the ramified fractals indicate the presence of Fe oxide species.

When the original sample fabricated in HPLC water was diluted 1/100 (v/v) and dried at 50 °C over 2 h for AFM observation, particular structures were observed. Figure 19 shows AFM images of ring-shaped self-organized NPs, consistent with a magnetic dipolar nature of NP interaction in which a nose-to-tail configuration minimizes the energy. Figure 19a shows a group of annular-shaped structures at the upper half of the panoramic view. Figure 19b is a close-up view showing isolat-

© 2017 Wiley-VCH Verlag GmbH & Co. KGaA, Weinheim

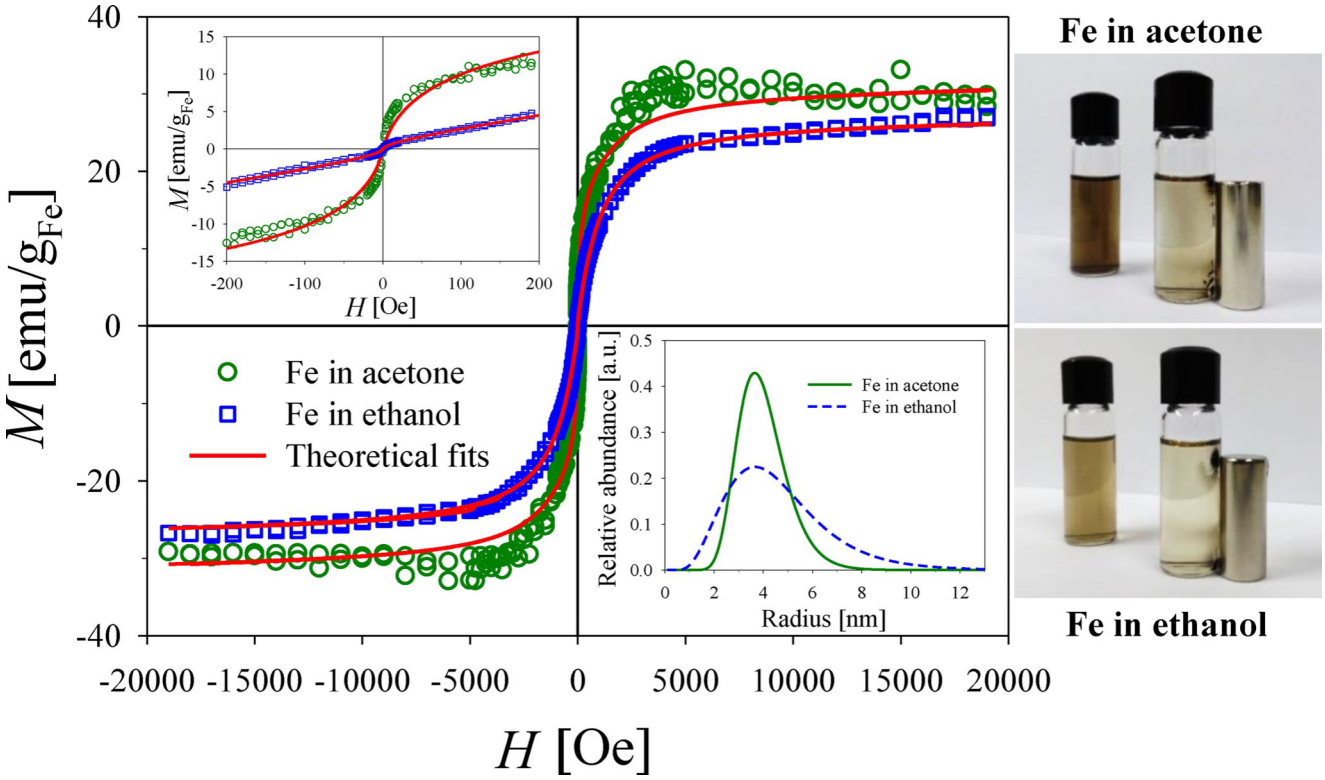

Figure 17. Magnetization curves for as-prepared iron colloids in acetone and ethanol obtained by laser ablation with 700 μJ pulse energy. Insets show an enlargement of the negligible hysteresis-cycle area at the origin (upper left) and the NP size distribution derived from curve fitting (lower right). Right: photographs of vials illustrating the magnetic-force effect on the NPs of an NdFeB magnet.

Table 3. Saturation magnetization M_S, magnetic moments $\langle\mu_1\rangle$ and $\langle\mu_2\rangle$, number densities N_1 and N_2, magnetic radii r_{1M} and r_{2M} and total radii r_{1T} and r_{2T} of colloidal Fe NPs, derived from VSM measurements in acetone and ethanol.

	Fe in acetone	Fe in ethanol
M_S [emu g_{Fe}^{-1}]	30.8 ± 0.8	26.5 ± 0.5
$\langle\mu_1\rangle$ [μ_B]	91297 ± 761	12473 ± 154
$\langle\mu_2\rangle$ [μ_B]	6518 ± 115	4467 ± 294
N_1 [g^{-1}]	1.3×10^{15}	1.9×10^{17}
N_2 [g^{-1}]	4.2×10^{17}	2.1×10^{17}
r_{1M} [nm]	3.4 ± 2.2	1.8 ± 0.4
r_{2M} [nm]	1.9 ± 0.4	1.8 ± 0.1
r_{1T} [nm]	20 ± 13	4 ± 2
r_{2T} [nm]	4 ± 1	5.2 ± 0.1

ed structures, one of which was selected for detailed measurements in a 3D view (Figure 19c). It seems to be composed of several NPs organized in an annular fashion, with a cross-sectional height profile of about 2 nm (Figure 19d).

2.5. Self-Organized Structures of Iron Colloids in Aqueous TSC Solution

A colloid in aqueous TSC solution was diluted 1/100 (v/v). A drop thereof was placed on a mica substrate and treated by the same drying process as for HPLC water. Figure 20 shows AFM images of ring-shaped self-organized NPs encountered in a certain zone of the drop. Figure 20a shows a group of these annular-shaped structures at the upper half of the panoramic view. This does not seem to be a particular case, but rather a frequent situation under certain experimental conditions. Figure 20c is a close-up view of a region in which two of these structures are seen. The transverse cross-sectional profile of one of them in the direction of the dashed line is shown in Figure 20d. Figure 20b shows the same image as Figure 20c but in phase mode, and indicates that the annular structures consist of a different material to the rest of the background.

3. Conclusions

UPLA was performed on pure Fe solid targets in four solvents at different pulse energies. Optical extinction spectra of the obtained colloids showed decreasing absorbance with decreasing pulse energy used for their fabrication, which suggests decreasing NP concentrations. The broad absorption peak in the range of 300–400 nm reported by other authors in ethanol was also observed in our experiments in water, aqueous citrate, and acetone for the three pulse energies used. These cases were not observed before.

Micro-Raman spectroscopic analysis of dried drops taken from the fabricated suspensions indicated that magnetite, maghemite, and hematite iron oxide phases are present in all four solvents. Raman spectra always showed mixtures of the bands assigned to each oxide phase, which suggest that the samples are quite heterogeneous in phase content.

© 2017 Wiley-VCH Verlag GmbH & Co. KGaA, Weinheim

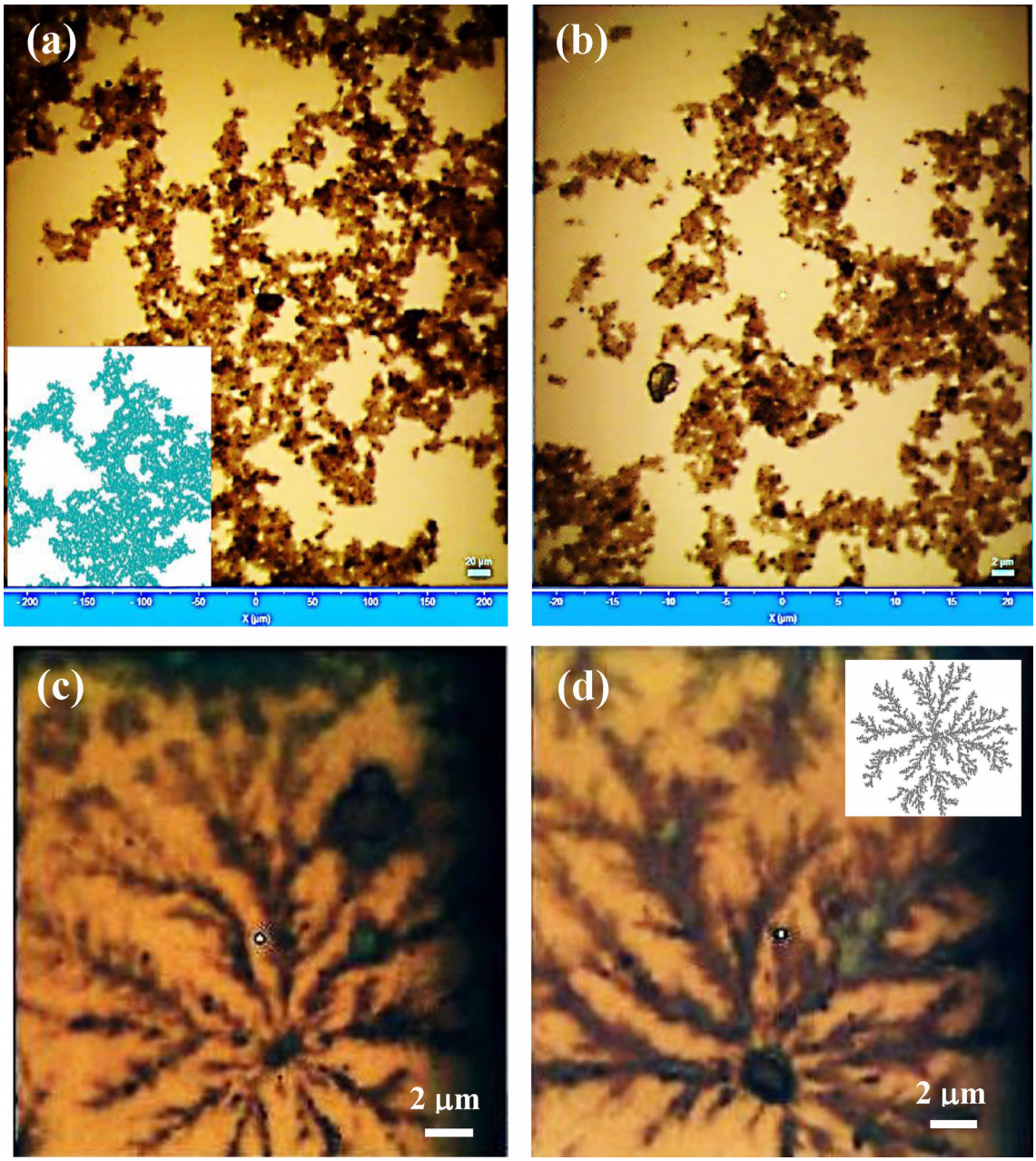

Figure 18. OM images of self-assembled colloidal Fe NPs in HPLC water. The scale bar in a) is 20 µm, and that in b) is 2 µm. The inset in a) is a simulation of a percolation fractal cluster. Scale bars in c) and d) are 2 µm. The inset in d) is a simulation of a ramified-growth fractal.

On a much smaller scale, TEM and AFM analyses showed that the NPs were spherical in shape, with some core–shell and hollow species. AFM size histograms yielded log-normal size distributions with modal radii in the range 2–4 nm depending on the solvent. HPLC water gave the narrowest (< 5 nm) distribution and acetone the widest (< 30 nm). ED patterns indicated a rather high degree of crystallinity of the NPs. The *q*-vector values of the different diffraction rings, recorded by ED, are compatible with Bragg planes corresponding to α-Fe, hematite, maghemite, and magnetite, in accordance with the phase results obtained by micro-Raman spectroscopy.

Magnetization measurements in HPLC water and aqueous citrate showed hysteresis loops with shape commonly observed for an assembly of magnetic NPs with randomly oriented magnetic-anisotropy axes. The low coercivity and remanent magnetization values found in the VSM experiments are in agreement with colloidal superparamagnetic behavior. Migration of the NPs in HPLC water towards a NdFeB magnet placed very close to the vial is a visual indication of their magnetic properties. Comparing magnetization curves for Fe magnetic NPs dispersed in organic solvents with those for Fe magnetic NPs dispersed in water shows that the former have a smaller high-field susceptibility, which indicates that the surface effects are minimized in the organically dispersed NPs, which is also consistent with larger NPs.

© 2017 Wiley-VCH Verlag GmbH & Co. KGaA, Weinheim

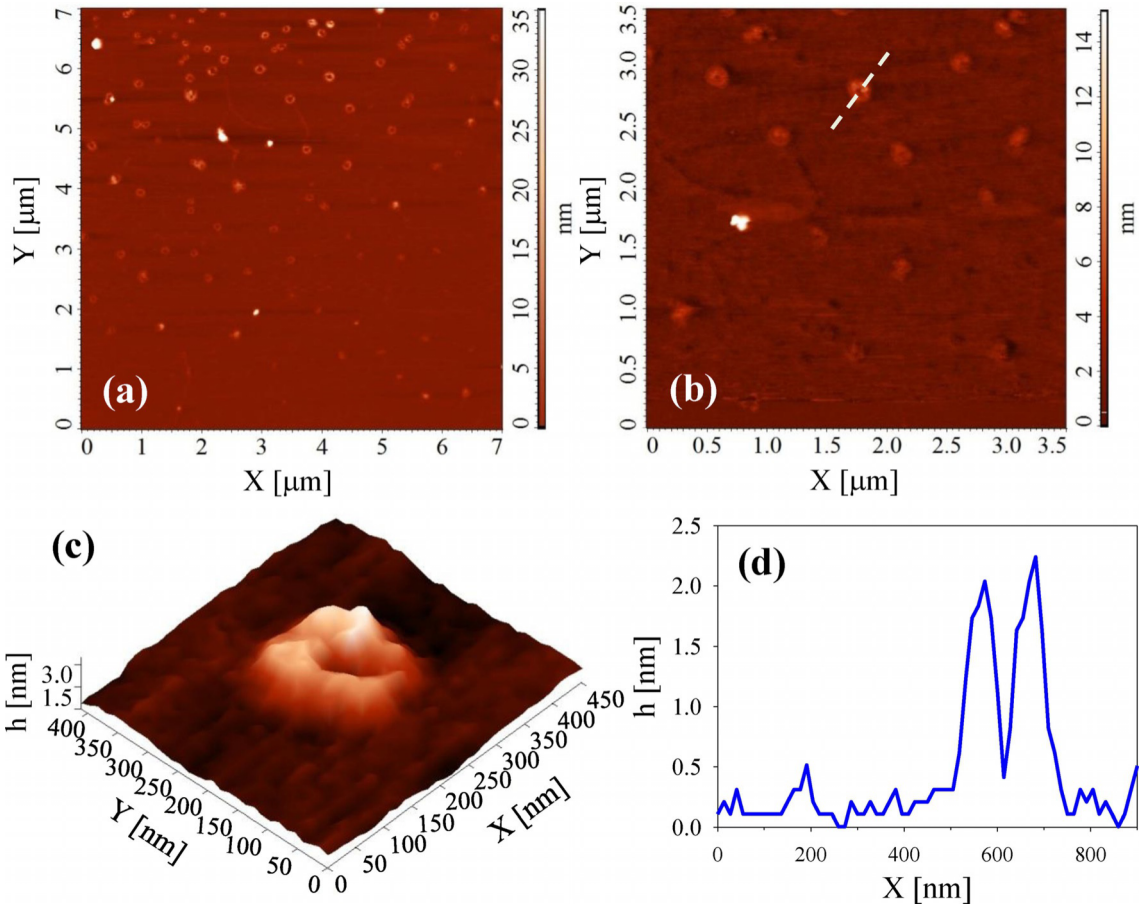

Figure 19. AFM images of ring-shaped self-organized NPs in HPLC water. a) Panoramic view, b) close-up view with some isolated structures, c) 3D view of a single isolated structure, and d) cross-sectional height profile.

For HPLC water and aqueous TSC, the mean magnetic moment and magnetic saturation of 49.3 emu g_{Fe}^{-1} and 26.7 emu g_{Fe}^{-1}, respectively, of the particles suggest that TSC acts as a surface modifier, decreasing the saturation magnetization by a surface spin disorder effect. In general, from the magnetization curves for Fe MNPs dispersed in organic solvents and those for Fe MNPs dispersed in water, it can be concluded that the former show a smaller high-field susceptibility, indicating that surface effects are minimized in the organically dispersed NPs. Size distributions derived from VSM analysis are in very good agreement with those derived from AFM measurements.

Finally, self-assembled 2D structures were observed in the samples prepared for Raman and AFM measurements. In the first case, percolation and ramified types of fractal growth of size in the micrometer range were observed at two different scales in dried-drop samples. Raman analysis performed on the fractals confirmed they are formed by Fe oxide NPs. On the other hand, AFM studies showed ring-shaped structures of about 2 nm height and a few hundred nanometers in diameter. These types of structures were found both in water and in aqueous TSC.

Acknowledgements

This work was Granted by PIP 0280 and PIP 0720 of CONICET, PME2006-00018 and 11/I197 (Facultad de Ingeniería), 11/X680 (Facultad de Ciencias Exactas) of Universidad Nacional de La Plata, Argentina. We thank C2NANO-Brazilian Nanotechnology National Laboratory (LNNano) and Brazilian Synchrotron Light Laboratory (LNLS) at Centro Nacional de Pesquisa em Energia e Materiais (CNPEM)/MCT (#19927 and #18425) for the use of TEM and the use of D01B-SAXS2 beam line for data acquisition under Proposal #13714. AFM was carried out at LFAyM and VSM of Instituto de Física La Plata (IFLP-CONICET). Fabrication of NPs by femtosecond laser ablation, OES, Raman, and OM studies were carried out at CIOp (CONICET- CICBA- UNLP), La Plata. We acknowledge Y-TEC S.A. for the use of TEM TALOS F200X under the supervision of Alejandra Floridia and Alberto Caneiro. We gratefully acknowledge their commitment and dedication. D.C.S. is a Member of Comisión de Investigaciones Científicas de la Provincia de Buenos Aires (CIC). L.B.S., M.B.F.v.R., and J.M.J.S. are researchers of CONICET, Argentina. D.M.A. is doctoral fellow of CONICET and D.F.C. is postdoctoral fellow of CONICET, Argentina. D.M. is Visiting Professor at the Universidade Federal do ABC, Centro de Ciencias Naturais e Humanas (CCNH).

© 2017 Wiley-VCH Verlag GmbH & Co. KGaA, Weinheim

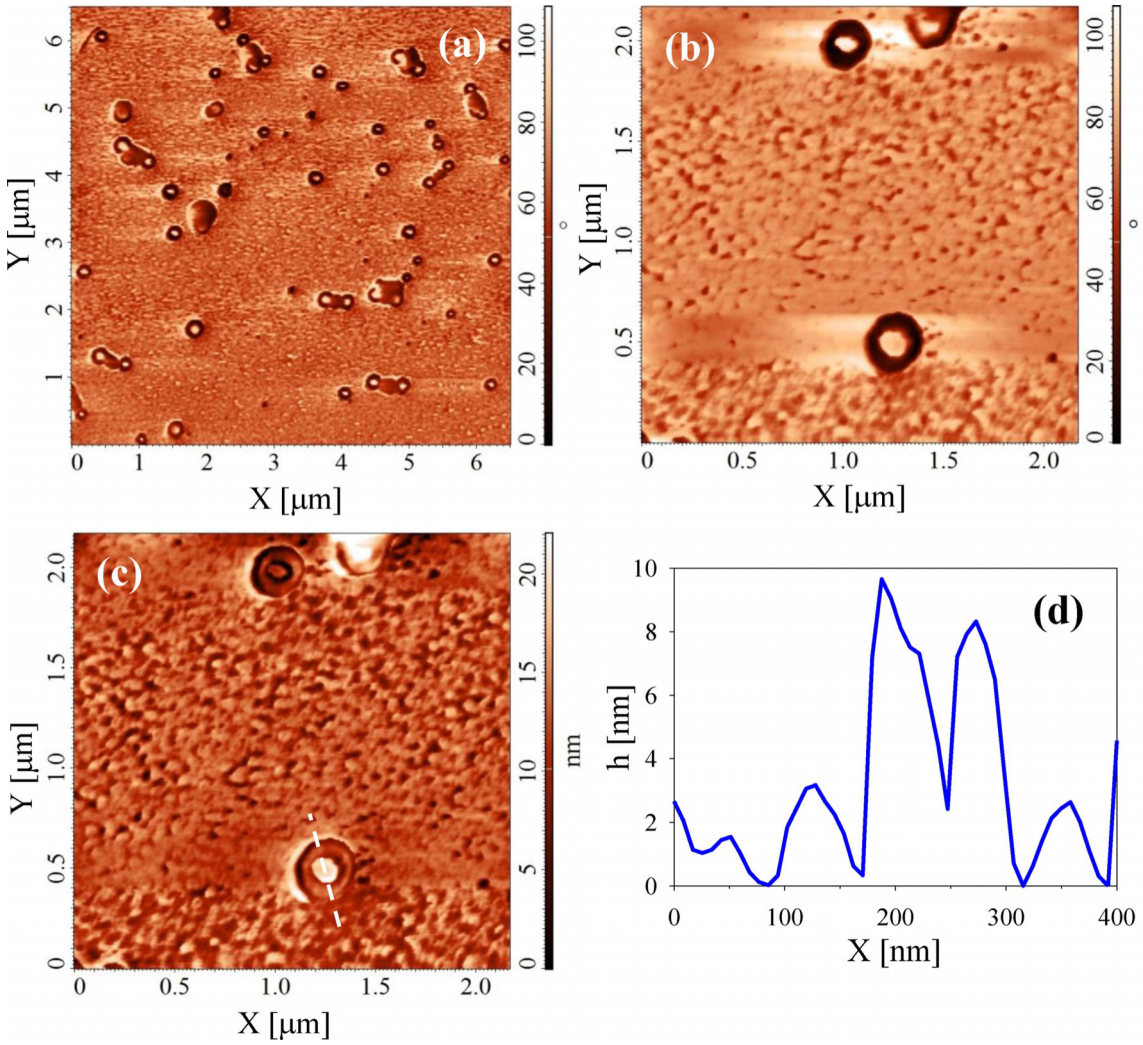

Figure 20. AFM phase-mode images of ring-shaped self-organized NPs. a) Panoramic view. b) Close-up view of a couple of isolated structures in phase mode. c) As b) but in height mode. d) Cross sectional height profile of the annular structure with dashed line in c).

Keywords: fractals · iron · laser ablation · magnetic properties · nanoparticles

[1] E. A. Périgo, G. Hemery, O. Sandre, D. Ortega, E. Garaio, F. Plazaola, F. J. Teran, *Appl. Phys. Rev.* **2015**, *2*, 041302.
[2] N. Landazuri, S. Tong, J. Suo, G. Joseph, D. Weiss, D. J. Sutcliffe, D. P. Giddens, G. Bao, W. R. Taylor, *Small* **2013**, *9*, 4017–4026.
[3] J. M. Orozco-Henao, D. F. Coral, D. Muraca, O. Moscoso-Londoño, P. Mendoza Zélis, M. B. Fernández van Raap, S. K. Sharma, K. R. Pirota, M. Knobel, *J. Phys. Chem. C* **2016**, *120*, 12796–12809.
[4] Y.-X. J. Wang, *Quant. Imaging Med. Surg.* **2011**, *1*, 35–40.
[5] O. Veiseh, J. W. Gunn, M. Zhang, *Adv. Drug Delivery Rev.* **2010**, *62*, 284–304.
[6] Y. Liu, G. Su, B. Zhang, G. Jiang, B. Yan, *Analyst* **2011**, *136*, 872–877.
[7] J. Liu, Z. Zhao, G. Jiang, *Environ. Sci. Technol.* **2008**, *42*, 6949–6954.
[8] "Synthesis, Properties and Biomedical Applications of Magnetic Nanoparticles", P. Tartaj, M. P. Morales, S. Veintemillas-Verdaguer, T. Gonzalez-Carreno, C. J. Serna in *Handbook of Magnetic Materials, Vol. 16* (Ed.: K. H. J. Buschow), Elsevier **2006**, pp. 403–482.
[9] M. Tominaga, M. Matsumoto, K. Soejima, I. Taniguchi, *J. Colloid Interface Sci.* **2006**, *299*, 761–765.
[10] T. Sugimoto, K. Sakata, *J. Colloid Interface Sci.* **1992**, *152*, 587–590.
[11] T. Sugimoto, K. Sakata, A. Muramatsu, *J. Colloid Interface Sci.* **1993**, *159*, 372–382.
[12] D. E. Zhang, Z. W. Tong, S. Z. Li, X. B. Zhang, A. L. Ying, *Mater. Lett.* **2008**, *62*, 4053–4055.
[13] C. Solans, P. Izquierdo, J. Nolla, N. Azemar, M. J. Garcia-Celma, *Curr. Opin. Colloid Interface Sci.* **2005**, *10*, 102–110.
[14] Z. Zhang, Q. Zhang, L. Xu, Y. Xia, *Synth. React. Inorg. Met.-Org. Nano-Met. Chem.* **2007**, *37*, 53–56.
[15] J. Pinkas, V. Reichlova, R. Zboril, Z. Moravec, P. Bezdicka, J. Matejkova, *Ultrason. Sonochem.* **2008**, *15*, 257–264.
[16] H. S. Desarkar, P. Kumbhakar, A. K. Mitra, *Laser Phys. Lett.* **2013**, *10*, 055903–055908.
[17] J. M. J. Santillán, F. A. Videla, M. B. Fernández van Raap, D. Muraca, L. B. Scaffardi, D. C. Schinca, *J. Phys. D* **2013**, *46*, 435301.
[18] P. Liu, W. Cai, H. Zeng, *J. Phys. Chem. C* **2008**, *112*, 3261–3266.
[19] Y. Vitta, V. Piscitelli, A. Fernandez, F. Gonzalez-Jimenez, J. Castillo, *Chem. Phys. Lett.* **2011**, *512*, 96–98.
[20] V. Amendola, P. Riello, S. Polizzi, S. Fiameni, C. Innocenti, C. Sangregorio, M. Meneghetti, *J. Mater. Chem.* **2011**, *21*, 18665–18673.
[21] V. Amendola, P. Riello, M. Meneghetti, *J. Phys. Chem. C* **2011**, *115*, 5140–5146.
[22] Y. Wei, B. Han, X. Hu, Y. Lin, X. Wang, X. Deng, *Procedia Eng.* **2012**, *27*, 632–637.
[23] P. Maneeratanasarn, T. Van Khai, S. Y. Kim, B. G. Choi, K. B. Shim, *Phys. Status Solidi A* **2013**, *210*, 563–569.
[24] V. Khare, A. Kraupner, A. Mantion, A. Jelicic, A. F. Thunemann, C. Giordano, A. Taubert, *Langmuir* **2010**, *26*, 10600–10605.

© 2017 Wiley-VCH Verlag GmbH & Co. KGaA, Weinheim

[25] I. V. Chernyshova, M. F. Hochella Jr, A. S. Madden, *Phys. Chem. Chem. Phys.* **2007**, *9*, 1736 – 1750.
[26] I. Chourpa, L. Douziech-Eyrolles, L. Ngaboni-Okassa, J.-F. Fouquenet, S. Cohen-Jonathan, M. Souce, H. Marchais, P. Dubois, *Analyst* **2005**, *130*, 1395 – 1403.
[27] T. S. Krishnan, *J. Indian Inst. Sci.* **1953**, *36*, Sec. A, PL XIII.
[28] C. H. Munro, W. E. Smith, M. Garner, J. Clarkson, P. C. White, *Langmuir* **1995**, *11*, 3712 – 3720.
[29] M. Kerker, O. Siiman, L. A. Bumm, D.-S. Wang, *Appl. Opt.* **1980**, *19*, 3253 – 3255.
[30] X. Li, D. W. Elliott, W. Zhang, *Crit. Rev. Solid State Mater. Sci.* **2006**, *31*, 111 – 122.
[31] J. M. J. Santillán, M. B. Fernández van Raap, P. Mendoza Zélis, D. Coral, D. Muraca, D. C. Schinca, L. B. Scaffardi, *J. Nanopart. Res.* **2015**, *17*, 1 – 13.
[32] D. Muñetón Arboleda, J. M. J. Santillán, L. J. Mendoza Herrera, M. B. Fernández van Raap, P. Mendoza Zélis, D. Muraca, D. C. Schinca, L. B. Scaffardi, *J. Phys. Chem. C* **2015**, *119*, 13184 – 13193.
[33] http://www.jems-saas.ch.
[34] J. Crangle, G. M. Goodman, *Proc. R. Soc. London. Ser. A, Math. Phys. Sci.* **1971**, *321*, 477 – 491.
[35] B. Sapoval, *Universalités et fractales*, Champs Flammarion, **2001**.
[36] T. A. Witten Jr, L. M. Sander, *Phys. Rev. Lett.* **1981**, *47*, 1400 – 1403.

Manuscript received: November 21, 2016
Revised: March 9, 2017
Accepted Article published: March 13, 2017
Final Article published: April 19, 2017

© 2017 Wiley-VCH Verlag GmbH & Co. KGaA, Weinheim